CHAPTER 4

METHODOLOGY

In earlier days, wind tunnels were the only tool for aerodynamic shape testing and design. In wind tunnels a parts of an aircraft or a complete aircraft or a scaled model is tested using force and pressure measuring equipment and modified as per design requirements. But wind tunnels are very costly and data fetching is time consuming. Nowadays Computational Fluid Dynamics (CFD) has emerged as a vital tool for aerodynamic design and shape optimization and is widely used in various spectrums of aerodynamic applications. Due to improvement in numerical algorithms and the rapid increase in computer speed and memory, the use of CFD has grown leaps and bounds as approximate results very close to actual values are readily obtained. As this research focuses on the minute geometric variations of the Busemann biplane and similar variations of Mach numbers, CFD has been used as the tool of experimentation. Fabrication of a large number of staggered and non-staggered biplanes for wind tunnel testing would have been quite expensive, while general academic supersonic tunnels operate at single Mach number. This makes the wind tunnel experiments unwarranted for this particular case where a large number of geometries are investigated at about 15 different Mach numbers. The CFD provides the inexpensive solution which order of accuracy for the selected Mach numbers.

4.1 Introduction to CFD

Computational Fluid Dynamics (CFD) plays an important tool for analyzing fluid dynamic problems through the solution of non-linear governing equations of fluid flows using numerical methods and algorithms. Computational Fluid Dynamics provides reasonably accurate solutions within the realm of approximate solution

and the results can be used for preliminary design and further integrated into the design along with validation studies. The steps involved in the analysis of a fluid dynamic problem using CFD includes following steps:

- Creation of geometry of the domain of interest for a problem.
- Division of the domain into smaller subdomains.
- Definition of the physical model to be used i.e. equations of motions.
- Definition of the boundary conditions, fluid behavior and the properties of the fluid.
- Solution of the governing equations through an iterative solver.
- Post Processing or the result analysis and flow visualization.

Different discretization approaches are used these days for CFD applications. There are in general three popular discretization schemes viz. finite difference (FD), finite volume (FV), and finite element method (FE). The oldest method of the three is the finite difference method for numerical solution of the partial differential equations. Such methods usually need structured grids, serving as local coordinate's lines. The Finite Volume method on the other hand, uses the integral form of the conservation equations, and the whole domain is divided into many sub-domains, i.e. control volumes. Conservation equations are applied to each control volume, and the node lies in the centre or the vertex of the cell where the variables are stored. The Finite volume method is suitable for complex geometries, which means it does not have restrictions on grid types. The disadvantage of this method is that higher order schemes are more difficult to implement in three dimensional cases. The Finite element method, as the third type of method, is similar to the Finite volume method. The physical domain is also reconstructed by discrete volumes (i.e. finite elements) that are generally unstructured. One of the important advantages is the ability to deal with arbitrary geometries. The Finite element method usually uses the unstructured mesh and the principle drawback is that the matrices of the linearized equations are not as well structured as those for structured grids. Therefore, it might have lower

efficiency. [44]

In general, the Finite difference method can be very effective and simple to perform the higher-order schemes with regular grids. The Finite element method has an ability to deal with arbitrary geometries and unstructured grid is usually used. The Finite volume method is the simpler to understand and program as compared to the finite element methods and similar to finite difference methods for structured grids. The Finite volume methods can be used for any type of grids, which is why it is popular for commercial CFD codes. This is the method used for the investigation in this thesis.

The control volume (i.e. the approach for FV method) deals with the flow in a certain spatial region. Fig. 4.1 shows the control volume and the typical notation used for two dimensional grids: a) vertex-centre based, b) cell-centre based. In the solver used in this work, the value of primitive and flux variables are stored at the cell centre [44]. For any conserved intensive property (i.e. mass, momentum, and energy) the integral form of the conservation equations for the numerical solution can be written as given by equation 4.1.

$$\frac{\partial}{\partial t}\int_{\Omega} \vec{U}\, d\Omega + \oint_{\partial\Omega}\left[\left(\bar{\bar{F}}_C - \bar{\bar{F}}_D\right)\cdot\vec{n}\right]\cdot dS = \int_{\Omega} \vec{Q}_v\, d\Omega + \oint_{\partial\Omega}\left(\bar{\bar{Q}}_S\cdot\vec{n}\right) dS \qquad (4.1)$$

or,

Rate of increase of fluid property inside the control volume	+	Net rate of decrease of fluid property due to convection across the control volume boundaries	=	Net rate of creation of fluid property inside the control volume	+	Net rate of increase fluid property due to diffusion across the control volume boundaries

The above equation represents that the rate of change of the amount of property in the control volume is the rate of change of the property within the control volume plus the net flux of it through the control volume boundary due to the fluid motion relative to the control boundary. In Eq.4.1 the term $\partial\Omega, dS$ denotes the boundaries of a control volume and a surface element, respectively, and $\vec{n}$ is outward going unit normal. The term $\vec{U}$ represents the column vector of unknown primitive or flux variables. In Equation 4.1, $\bar{\bar{F}}_C$ and $\bar{\bar{F}}_D$ represents the convective and diffusive

flux tensors respectively while the term $\vec{Q}_v$ stands for the local sources inside the volume, and $\bar{\bar{Q}}_S$ means surface source tensor. [44]

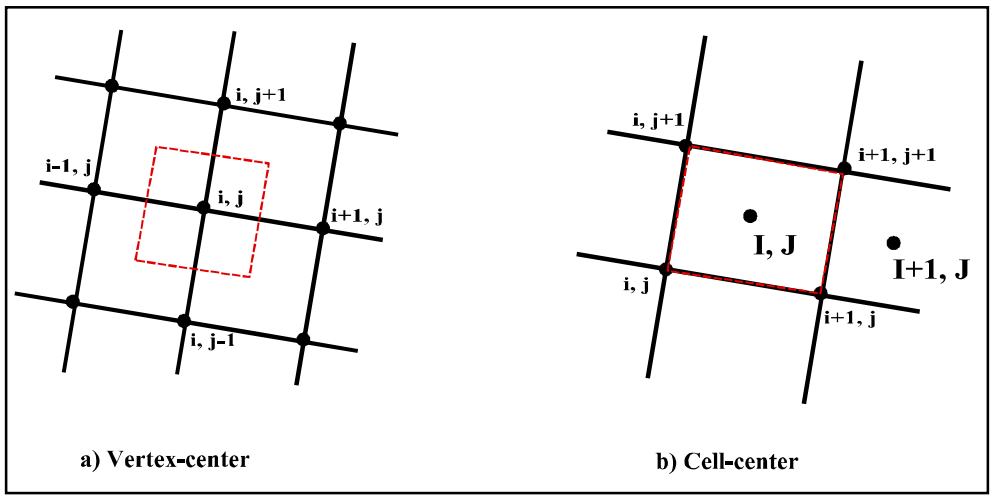

Fig.4.1: Schematic of two-dimensional control volumes grids [44]

4.2 Governing equations

The equation of the fluid dynamics is the well-known Navier-Stokes equations that come directly from the conservation laws of mass, momentum, and energy. The integral form of the mass, momentum conservation equation follows directly from the general equation (Eq. 4.1).

For continuity, Eq. 4.1 can be rearranged into:

$$\frac{\partial}{\partial t}\int_{\Omega} \rho \, d\Omega + \oint_{\partial\Omega} \rho \, (\vec{v} \cdot \vec{n}) \, dS = 0 \tag{4.2}$$

The first term in Eq. 4.1 represents the time rate of increase in total mass inside the finite control volume Ω, and the second term denotes the net mass flow out of the control volume, and the positive mass flow corresponds to outflow and negative to inflow. By applying the Gauss's divergence theorem to the convection term, the surface integral can be written into a volume integral, therefore, Eq. 4.1 can be written into the differential form:

$$\frac{\partial \rho}{\partial t} + \ div\,(\rho v) = 0 \tag{4.3}$$

For a given coordinate system, Eq. 4.3 can be expressed using the divergence operator into the particular coordinate system. Hence, as an example, the Eq. 4.3 can be reformulated into the Cartesian coordinate system:

$$\frac{\partial \rho}{\partial t} + \frac{\partial (\rho u)}{\partial x} + \frac{\partial (\rho v)}{\partial y} + \frac{\partial (\rho w)}{\partial z} = 0 \tag{4.4}$$

where $u, v, and\ w$ in Eq. 4.4 denote as the velocity components in *x*, *y*, and *z* direction.

The equations for the momentum, consistent with the generic integral form of Eq. 4.1 can be given by equation 4.5.

$$\frac{\partial}{\partial t}\int_{\Omega} \rho \vec{v}\, d\Omega + \oint_{S} \rho \vec{v}\,(\vec{v}.\vec{n})\, dS = \int_{\Omega} \rho\, f_e d\Omega - \oint_{S} p\,\vec{n}\, dS + \oint_{S} \left(\overline{\overline{\tau}}\,\vec{n}\right) dS \tag{4.5}$$

The left hand side of Eq. 4.5 represents the time rate changing of momentum due to the unsteadiness of the flow properties inside the control volume, and the second term means the net flow of momentum out of the control volume across the surface S. The term $\int_{\Omega} \rho\, f_e d\Omega$ in above equation represents the body forces, while the second, third terms are the sum of pressure forces, and the viscous forces acting on the flow as it across the control surfaces respectively. The surface forces are the forces which act due surface contact such as pressure, normal and shear stress, surface tension, etc. while the body forces are forces such like gravity, centrifugal, and Coriolis forces, and electromagnetic forces which act from a distance.

The energy equation is the statement the first law of thermodynamics applied to a finite control volume of fluid. The first law of thermodynamics states, "*the time rate of change in the total energy inside a control volume is the sum of the rate of work done by surface and body forces acting on the control volume and rate of*

heat addition into it". For a thermally perfect gas under equilibrium conditions, the total specific energy at any point in the control volume of a fluid is the sum its specific internal energy and its specific kinetic energy, and can be written as Eq. 4.6.

$$E = e + \frac{V^2}{2} = e + \frac{u^2 + v^2 + w^2}{2} \tag{4.6}$$

The time rate of change of the energy flux ρE, within a finite control volume Ω due to flow unsteadiness can be given by Eq. 4.7.

$$\frac{\partial}{\partial t} \int_{\Omega} \rho E \, d\Omega \tag{4.7}$$

The flux of total energy through the control surfaces of the domain occurs due to both the diffusive and convective phenomena. The diffusion of thermal energy, called as conduction is directly proportional to the temperature gradient in the flowfield and is given by Fourier's Law as written as Eq. 4.8.

$$\vec{F}_D = -k \nabla T \tag{4.8}$$

where k is the local thermal conductivity of the fluid.

Another means of heat addition to the control volume are the internal sources like the chemical reactions, radiation, irradiation or electrical sources of heating. The volumetric heating rate $\dot{q}_h$ due to heat sources and the work done by body forces per unit time can be combined as total contribution from volumetric sources and given as

$$Q_V = \rho \overrightarrow{f_e} . \vec{v} + \dot{q}_h \tag{4.9}$$

In Eq. 4.9 $\overrightarrow{f_e}$, is the body force vector acting per unit mass of the fluid volume.

The contributions from the work done, per unit time, by the surface forces viz. the

pressure and viscous stresses account for a major component of the energy conservation and is given by Eq. 4.10.

$$\vec{Q}_S = -p\vec{v} + \bar{\bar{\tau}}.\vec{v} \tag{4.10}$$

where $\bar{\bar{\tau}}$ represents the viscous stress tensor. Combining the heat fluxes from all the sources and the rate of work done by all the forces, the energy equation can be written as Eq. 4.11

$$\frac{\partial}{\partial t}\int_{\Omega}\rho E d\Omega + \oint_{d\Omega}\rho E(\vec{v}.\vec{n})dS = \oint_{\partial\Omega} k(\nabla T.\vec{n})dS + \int_{\Omega}\left(\rho\vec{f}_e.\vec{v} + \dot{q}_h\right)d\Omega - \oint_{d\Omega} p(\vec{p}.\vec{n})dS + \oint_{d\Omega}\left(\overline{\overline{\tau.\vec{v}}}\right).\vec{n}dS \tag{4.11}$$

4.5 Navier-Stokes Equation: Vector-variable form

For the numerical solution of the fluid flows it is convenient to arrange all the equations in vector-variable form. The vector integral form of governing equation, with convective and viscous flux vectors split out can be written as Eq. 4.12.

$$\frac{\partial}{\partial t}\int_{\Omega}\vec{W}\,d\Omega + \oint_{S}\left(\vec{F}_c - \vec{F}_v\right)dS = \int_{\Omega}\vec{Q}\,d\Omega \tag{4.12}$$

where the vector of the conserved variables, and the fluxes are listed as follows:

$$\overrightarrow{\mathrm{W}} = \begin{bmatrix}\rho\\ \rho u\\ \rho v\\ \rho w\\ \rho E\end{bmatrix}, \quad \overrightarrow{F_c} = \begin{bmatrix}\rho V\\ \rho uV + n_x p\\ \rho uV + n_y p\\ \rho uV + n_z p\\ \rho HV\end{bmatrix}, \overrightarrow{F_v} = \begin{bmatrix}0\\ n_x\tau_{xx} + n_y\tau_{xy} + n_z\tau_{xz}\\ n_x\tau_{yx} + n_y\tau_{yy} + n_z\tau_{yz}\\ n_x\tau_{zx} + n_y\tau_{zy} + n_z\tau_{zz}\\ n_x\Theta_x + n_y\Theta_y + n_z\Theta_z\end{bmatrix} \tag{4.13}$$

The contravariant velocity, U, in Eq. 4.13 is expressed as following:

$$V = \vec{v} \cdot \vec{n} = un_x + vn_y + wn_z$$

The elements of the shear stress tensor as proved by Stokes can be given by equation 4.14.

$$\tau_{xy} = \frac{2}{3}\mu\left(2\frac{\partial u}{\partial x} - \frac{\partial v}{\partial y} - \frac{\partial w}{\partial z}\right)$$

$$\tau_{yy} = \frac{2}{3}\mu\left(2\frac{\partial v}{\partial y} - \frac{\partial u}{\partial x} - \frac{\partial w}{\partial z}\right)$$

$$\tau_{zz} = \frac{2}{3}\mu\left(2\frac{\partial w}{\partial z} - \frac{\partial u}{\partial x} - \frac{\partial v}{\partial y}\right)$$

$$\tau_{xy} = \tau_{yx} = \mu\left(\frac{\partial u}{\partial y} + \frac{\partial v}{\partial x}\right) \qquad (4.14)$$

$$\tau_{xz} = \tau_{zx} = \mu\left(\frac{\partial w}{\partial x} + \frac{\partial u}{\partial z}\right)$$

$$\tau_{yz} = \tau_{zy} = \mu\left(\frac{\partial v}{\partial z} + \frac{\partial w}{\partial y}\right)$$

4.6 Turbulence and transitional models

The three dimensional flows are highly unsteady and most of them are turbulent. In turbulent flow, the fundamental flow properties fluctuates and this makes the numerical simulation very difficult. Although the smallest of fluctuations can be simulated through the solution of unsteady Navier Stokes equations, it requires infinitesimally small distance between the nodes and also infinitesimally small time step for unsteady computations. The computational power requirements for these so called Direct Numerical Simulations are so large that such simulations cannot be performed for any practical aerodynamic problems even with the most efficient computers on the planet. Resolving only the large scale turbulence with Large Eddy Simulations (LES) is slightly less computationally expensive but still out of reach for large number of design modifications. The RANS and URANS

(i.e. Unsteady/Reynolds-averaged Navier-Stokes) methods, where the turbulent stresses are modeled with approximate formulations provide reasonably good results for turbulent flows and are computationally cheaper. The RANS method is based on the time averaging of flux variables and the flow is statistically steady.

4.6.1 Turbulence equations

The unsteady Navier-Stokes equations as written in Equation 4.15 in vector notation are capable of resolving all scales of turbulence.

$$\frac{\partial \rho}{\partial t} + \frac{\partial}{\partial x_i}(\rho v_i) = 0$$

$$\frac{\partial}{\partial t}(\rho v_i) + \frac{\partial}{\partial x_j}(\rho v_j v_i) = -\frac{\partial p}{\partial x_i} + \frac{\partial \tau_{ij}}{\partial x_j} \qquad (4.15)$$

$$\frac{\partial}{\partial t}(\rho E) + \frac{\partial}{\partial x_j}(\rho v_j H) = \frac{\partial}{\partial x_j}(v_i \tau_{ij}) + \frac{\partial}{\partial x_j}\left(k \frac{\partial T}{\partial x_j}\right)$$

In Eq. 4.15, the subscript *i* represents a component in *i*-direction while subscript on derivative represents summation through all three directions. The viscous stress tensor τ_{ij} is a second order tensor of velocity gradients wherein each element is given as follows

$$\tau_{ij} = 2\,\mu\, S_{ij} + \lambda \frac{\partial v_k}{\partial x_k}\delta_{ij} = 2\,\mu\, S_{ij} - \left(\frac{2\mu}{3}\right)\frac{\partial v_k}{\partial x_k}\delta_{ij}$$

In above equation, $\delta_{i,j}$ is the kronecker delta operator which has non zero values only when $i=j$ and the strain-rate tensor are given by

$$S_{ij} = \frac{1}{2}\left(\frac{\partial v_i}{\partial x_j} + \frac{\partial v_j}{\partial x_i}\right)$$

and the rotation-rate tensor is given by

$$\Omega_{ij} = \frac{1}{2}\left(\frac{\partial v_i}{\partial x_j} - \frac{\partial v_j}{\partial x_i}\right)$$

In Eq. 4.15, the total energy E and the total enthalpy H are respectively given by the following expressions

$$E = e + \frac{1}{2} v_i v_i, \qquad H = h + \frac{1}{2} v_i v_i$$

4.4.2 Reynolds Averaging

Understanding turbulent flows has been one of the most challenging problems faced by physicist and engineers of the 20th century. A method to accommodate the effects of turbulence on the flow characteristic was suggested by Reynolds in 1895 and it still finds applicability in numerous engineering applications. For turbulent flows, the primitive flow variables are decomposed into two components wherein the first part is a mean value of the variable over a small interval of time and the second part is the fluctuation of the variable as written in Eq. 4.16.

$$v_i = \bar{v}_i + v_i' \qquad p = \bar{p} + p' \tag{4.16}$$

The mean values in Eq. 4.16 can be obtained through one the following averaging procedures.

i. Time averaging

$$\bar{v}_i = \lim_{T' \to \infty} \frac{1}{T'} \int_t^{t+T'} v_i dt \tag{4.17}$$

In time averaging, the mean value of $\bar{v}_i$ does not vary in time, but only in space as shown in Fig. 4.2. In Eq. 4.17, $T \to \infty$ represents a time interval that is large as

compared to the time scale of the turbulent fluctuations. This averaging is useful for estimating steady state turbulence.

ii. Spatial averaging

$$\bar{v}_i = \lim_{\Omega \to \infty} \frac{1}{\Omega} \int_{\Omega} v_i d\Omega \tag{4.18}$$

In spatial averaging the variables are averaged over a control volume such that the mean value $\bar{v}_i$ is uniform in space, but may change with time. This averaging is useful for computing homogenous turbulence.

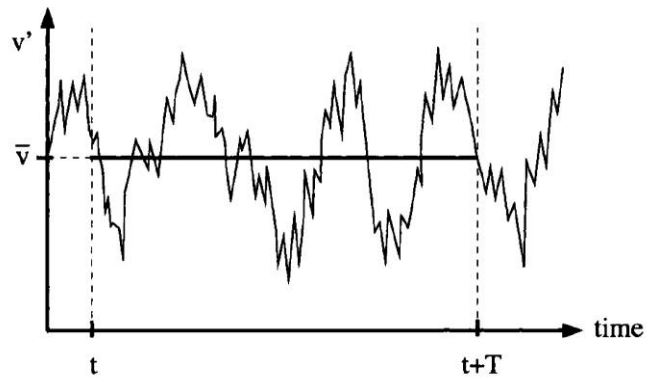

Fig. 4.2: Fluctuations of velocity over time in a turbulent flow

iii. Ensemble averaging

$$\bar{v}_i = \lim_{N \to \infty} \frac{1}{N} \sum_{m=1}^{N} v_i \tag{4.19}$$

In ensemble averaging, the mean value $\bar{v}_i$ averaged both over space and time and is appropriate for modeling general turbulence. In all of the above averaging methods, the mean of the fluctuating component is zero, i.e. $\bar{v}_i^{/} = 0$, however, the mean of the product of the fluctuations of two components is non-zero, i.e. $\overline{v_i' v_j'} \neq 0$.

4.4.3 Favre (Mass) – Averaging

In compressible flows wherein density is highly variable, the Reynolds averaging does not provide high fidelity computation of turbulence effects as in Reynolds averaging of variables an additional correlation for density fluctuations are required which complicates the computations. To alleviate this, a common practice is to perform mass weighted averaging of the certain flow variables. Generally the Reynolds averaging is implemented for density and pressure, while the mass (Favre) averaging is preferred for variables like velocity, enthalpy and temperature. Mass averaging of a flowfield variable can be written as Eq. 4.20.

$$\overline{v}_i = \frac{1}{\overline{\rho}} \lim_{T \to \infty} \frac{1}{T} \int_t^{t+T} \rho v_i dt \tag{4.20}$$

where $\overline{\rho}$ denotes the Reynolds-averaged density. Thus for the mass averaged decomposition a variable can be given as

$$v_i = \overline{v}_i + v_i'' \tag{4.21}$$

As with Reynolds averaging, the average of the fluctuating part is zero i.e. $\widetilde{v}_i'' = 0$ and the average of the product of the two fluctuating quantities is not zero, if the quantities are correlated.

4.4.4 Favre and Reynolds Averaged Navier-Stokes Equations

Often in turbulence modeling, it assumed that Morkovin's hypothesis is valid which says, "the turbulent structure of a boundary layer is not notably influenced by density fluctuations if $\rho' << \overline{\rho}$". The Morkovin's hypothesis is holds true for wall-bounded subsonic and supersonic flows. However, for hypersonic flows or the free shear layers in compressible flows, the density fluctuations are taken into account.

Reynolds averaging of the variable like density and pressure, and the Favre averaging to the remaining flow variables in the compressible Navier-Stokes

equations yields the so called Reynolds averaged Navier-Stokes equations as given in Eq. 4.22.

$$\frac{\partial \overline{\rho}}{\partial t} + \frac{\partial}{\partial x_i}\left(\overline{\rho}\widetilde{v}_i\right) = 0$$

$$\frac{\partial}{\partial t}\left(\overline{\rho}\widetilde{v}_i\right) + \frac{\partial}{\partial x_j}\left(\overline{\rho}\widetilde{v}_j\widetilde{v}_i\right) = -\frac{\partial \overline{p}}{\partial x_i} + \frac{\partial}{\partial x_j}\left(\overline{\tau}_{ij} - \overline{\rho}\overline{v_i'' v_j''}\right) \tag{4.22}$$

$$\frac{\partial}{\partial t}\left(\overline{\rho}\widetilde{E}\right) + \frac{\partial}{\partial x_j}\left(\overline{\rho}\widetilde{v}_j\widetilde{H}\right) = \frac{\partial}{\partial x_j}\left(k\frac{\partial \widetilde{T}}{\partial x_j} - \overline{\rho}\overline{v_j'' h''} + \overline{\tau_{ij} v_i''} - \overline{\rho}\overline{v_j'' K}\right) + \frac{\partial}{\partial x_j}\left[\overline{v}_i\left(\overline{\tau}_{ij} - \overline{\rho}\overline{v_i'' v_j''}\right)\right]$$

In Eq. 4.22, the viscous stress tensors in the momentum and energy equations are replaced by the Favre-averaged Reynolds-stress tensor, i.e.

$$\tau_{ij}^{F} = -\overline{\rho}\overline{v_i'' v_j''}$$

Similarly the Favre-averaged turbulent kinetic energy is given by

$$\overline{\rho}\widetilde{K} = \frac{1}{2}\overline{\rho}\overline{v_i'' v_j''}$$

and the total energy can be expressed thereafter as

$$\overline{\rho}\widetilde{E} = \overline{\rho}\widetilde{e} + \frac{1}{2}\overline{\rho}\widetilde{v}_i\widetilde{v}_i + \frac{1}{2}\overline{\rho}\overline{v_i'' v_i''} = \overline{\rho}\widetilde{e} + \frac{1}{2}\overline{\rho}\widetilde{v}_i\widetilde{v}_i + \overline{\rho}\widetilde{K}$$

Finally, the total enthalpy is defined as

$$\overline{\rho}\widetilde{H} = \overline{\rho}\widetilde{h} + \frac{1}{2}\overline{\rho}\widetilde{v}_i\widetilde{v}_i + \frac{1}{2}\overline{\rho}\overline{v_i'' v_j''} = \overline{\rho}\widetilde{h} + \frac{1}{2}\overline{\rho}\widetilde{v}_i\widetilde{v}_i + \overline{\rho}\widetilde{K}$$

In the Favre and Reynolds-averaged Navier-Stokes Eq. 4.22, the term $\frac{\partial}{\partial x_j}\left(k\frac{\partial \widetilde{T}}{\partial x_j}\right)$ represents conduction of heat, the term $\frac{\partial}{\partial x_j}\left(\overline{\rho}\overline{v_j'' h''}\right)$ represents the transport of specific enthalpy due turbulence, the term $\frac{\partial}{\partial x_j}\left(\overline{\tau_{ij} v_i''}\right)$ represents

molecular diffusion of the turbulent kinetic energy $\tilde{K}$, the term $\frac{\partial}{\partial x_j}\left(\bar{\rho}\overline{v_j'' K}\right)$ represents turbulent transport of the kinetic energy $\tilde{K}$, $\frac{\partial}{\partial xj}\left(\tilde{v}_i \tilde{\tau}_{ij}\right)$ represents work done by the viscous stresses due to molecular diffusion, $\frac{\partial}{\partial xj}\left(\tilde{v}_i \tau_{ij}^F\right)$ represents work done by the Favre-averaged Reynolds stresses,

The molecular diffusion and turbulent transport of $\tilde{K}$ are very often neglected for the transonic and supersonic flows while these terms are significant for hypersonic and high temperature flows.

There are various turbulence models that have been developed for approximation of the effect of turbulence in the numerical simulation of engineering fluid flows. The Spalart-Allamaras turbulence models are selected for this research project and the details of the models are described in next section. [44]

4.6 Turbulent Modelling

Turbulence is the unsteady, irregular motion of fluid particle in which transported quantities fluctuate in time and space. Turbulent modeling plays and important role in the computation of high Reynolds' number flows.

While performing the RANS simulation the turbulent models play an important role for the detailed study for turbulent flows. The large scale turbulence is produced due to the shock-boundary layer interaction and boundary layer separation in the flowfield; hence the correct choice of the turbulence model is necessary for the prediction of turbulence in the flowfield.

In the current research Spalart-Allmaras (S-A) turbulence model is used to predict the turbulence in the flowfield. One equation model such as Spalart-Allmaras model seems to be good compromise between algebraic and two equation models. Spalart-Allmaras model directly solves the transport equation for the eddy viscosity and has become very popular for reasonably correct results with lesser

cost for aerodynamic flows. This model also provides good results for the transport of turbulent flow in complex industrial configuration. [55, 56, 57, 58, 59]

The transport equation for the modified turbulent viscosity, $\bar{v}$ solved for the S-A model is given by equation 4.23. $\bar{v}$ [55].

$$\frac{\partial \bar{v}}{\partial t} + \bar{u}_j \frac{\partial \bar{v}}{\partial x_j} = c_{b1}\bar{S}\bar{v} + \frac{1}{\sigma}\left[\frac{\partial}{\partial x_j}\left((v+\bar{v})\frac{\partial \bar{v}}{\partial x_j}\right) + c_{b2}\frac{\partial \bar{v}}{\partial x_j}\frac{\partial \bar{v}}{\partial x_j}\right] - c_{w1}f_w\left(\frac{\bar{v}}{d}\right)^2 \qquad (4.23)$$

The eddy viscosity is then defined as:

$$\mu_t = \bar{\rho}\bar{v}f_{v1} = \bar{\rho}v_t$$

A damping factor f_{v1} is defined in order to ensure that $\bar{v} = kyu_t$ in the log layer and viscous sub-layer as:

$$f_{v1} = \frac{\chi^3}{\chi^3 + c_{v1}^3} \quad with\ \chi = \frac{\bar{v}}{v}$$

The vorticity magnitude S is modified such that $\bar{S}$ maintain its log-layer behaves

$$\left(\bar{S} = \frac{u_t}{k_y}\right)$$

$$\bar{S} = \sqrt{2\Omega_{ij}\Omega_{ij}}f_{v3} + \frac{\bar{v}}{k^2d^2}f_{v2}$$

$$\Omega_{ij} = \frac{1}{2}\left(\frac{\partial \bar{u}_i}{\partial x_j} - \frac{\partial \bar{u}_j}{\partial x_i}\right)$$

which is accomplished with help of the function

$$f_{v2} = 1 - \frac{\chi}{1+\chi f_{v1}}, \qquad f_{v3} = 1.$$

In order to obtain a faster decaying behavior of destruction in the outer region of the boundary layer, a function f_w is used:

$$f_w(g) = g\left(\frac{1+c_w^6}{g^6 + c_{w3}^6}\right)^{1/6}, \quad g = r + c_{w2}(r^6 - r), \quad r = \frac{\bar{v}}{\bar{S}k^2d^2}$$

Both r and f_w are equal to 1 in log-layer and decreases in the outer layer. Constants of the model are [55]:

$$c_{b1} = 0.1355, \quad c_{b2} = 0.622, \quad \sigma = \frac{2}{3}, \quad k = 0.41$$

$$c_{w1} = \frac{c_{b1}}{k^2} + \frac{1 + c_{b2}}{\sigma}, \quad c_{w2} = 0.3, \quad c_{w3} = 2, \quad and \; c_{v1} = 0.71$$

4.8 Geometric Modelling and Grid Generation

4.6.1 Geometric Modelling

Geometric modelling is the mathematical description of different shapes is used for engineering application for studying the different parameters. For the current study the different airfoil geometries are used and are shown in Fig.4.3.

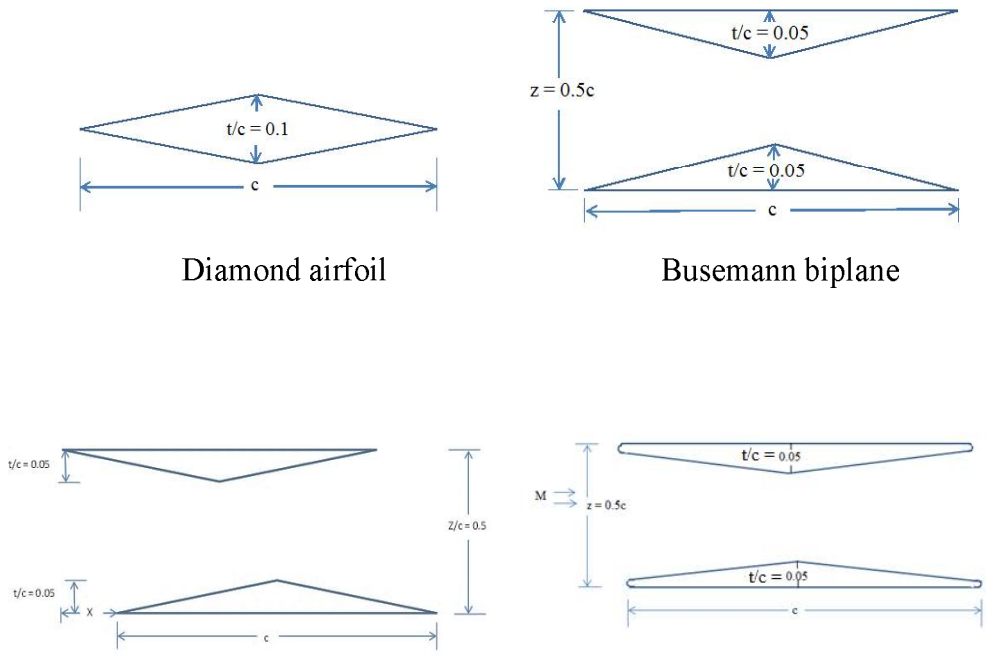

Diamond airfoil

Busemann biplane

Staggered Biplane

Biplane with Leading and Trailing edge radius

Fig. 4.3: Basic geometries

where c is the chord, t/c is thick to chord ratio, z is the distance between the Busemann elements, 'x' is the stagger between the elements and 'r' is the radius

of leading edge and trailing edge of the upper and lower elements. The values of all the variables used for the current study is given in the Table 4.1.

4.6.2 Grid Generation

A grid is a small-sized geometrical shape that covers the physical domain, whose objective is to identify the discrete volumes or elements where conservation laws can be applied. Grid generation is the first process involved in computing numerical solutions to the equations that describe a physical process. The result of the solution depends upon the quality of grid. A well-constructed grid can improve the quality of solution whereas, deviations from the numerical solution can be observed with poorly constructed grid.

Table 4.1 values of the variables used in basic geometries.

	Values
Chord (c)	1 m
Thickness/chord (t/c)	10%
Distance between biplane elements (z)	50% c
Stagger Distance (x)	10% c, 20% c, 30% c, 40% c, 50% c
Radius of leading edge and trailing edge (r)	1mm, 2mm, 3mm, 5mm

For the numerical solution of the governing equations of fluid flow, the flow domain must be discretized i.e., divided into a number of cells or grid points where the solution can be obtained. Numerical solutions are often represented as discrete values of a quantity at the grid points, or as the average of the quantity over one cell as shown in Fig. 4.4.

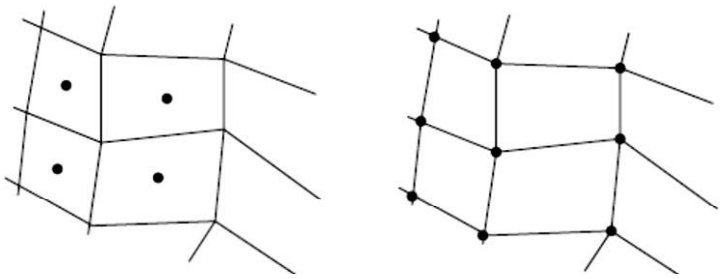

Fig. 4.4: Grid points and cell centers.

The more closely packed the grid points are, the more is the accuracy of the solution for a given algorithm and order of accuracy of the schemes. With finer meshes however, the time steps for marching have to be very small which means a larger computational time for same level of accuracy. Also with a large number of cells or grid points, the computer memory requirements increase which increases the computational time required for each iteration. This further delays the solution procedure. For the finest of grids required for most accurate solutions of real life engineering problems the computational capacities of even the modern supercomputers are insufficient. So a compromise has to be exercised between accuracy and the computational time requirements. Besides the fineness of the grid another aspect of grid generation for discretization of a complex geometry, is the choice of either structured or unstructured grids.

Unstructured grids: In unstructured grid generation, the domain is divided into small polygons, quadrilaterals and often triangles as shown in Fig. 4.5. In the computer data structure, each triangle has pointers to its neighbors and inform about their connectivity and the triangles/quadrilaterals are numbered in a random fashion. The coordinates of the vertices and the centroid of each polynomial are however is stored in an array. Unstructured meshes are often associated with the finite element discretization, but these are often used for finite volume techniques as well by considering each cell as finite volume wherein the conservation laws hold.

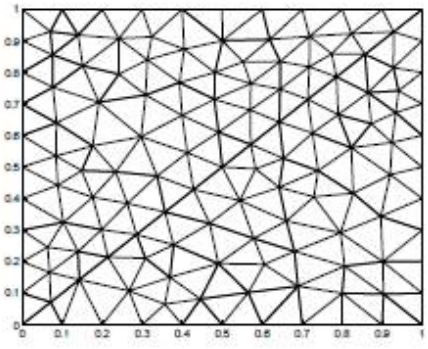

Fig. 4.5: Unstructured triangular mesh on a unit square

The major advantages of the unstructured grids are that block decomposition is not required for the parallel implementations and the refinement of the mesh is also straightforward. The disadvantages of unstructured grid are that it is inefficient on many computer architectures and getting an efficient parallelization is not straightforward and the discretization formulas are often more complicated.

Structured grids: Structured grids are the ones wherein the grid points are indexed in a regular fashion along coordinate directions. Structured grid can be thought of a mapping from physical plane to computational plane given by equation 4.24.

$$x = x(\xi,\eta,\zeta), y = y(\xi,\eta,\zeta), z = z(\xi,\eta,\zeta) \tag{4.24}$$

In the finite difference method, the solution is obtained over a rectangular or a cubic grid in the computational plane which is obtained through the transformation in 4.24. The same transformation is used to transform the derivatives and governing equations to the computational plane. It is possible to define finite volume or finite difference approximations which do not require smoothness of the grid, but these approximations are in general more complex and computationally expensive.

The major advantages in using structured grids are that it is quite easy to implement the computational algorithms as the grids are indexed and does not require the connectivity information. As the structured grids are often orthogonal, these provide high fidelity solutions to the numerical problem. The major disadvantages with the structured grids are that it is quite difficult to discretize a complex domain using this method as a smooth transformation for a complex geometry might not always be available. Another aspect is the problem associated with the grid refinements, as the structured nature of the grids is lost during an adaptive refinement. The difficulties associated with complex domains are often alleviated with the use of multi-block structured grids which is however a tiring process and requires large man hours and even might not always be feasible. The

individual blocks in the grid can be arranged either in adjacent positions as shown in Fig. 4.6 (a) or overlapping one another as shown in Fig. 4.6(b). In both the cases special interpolating boundary conditions are required at the interfaces between the grids. If a single polar coordinate system is used, the grid mapping becomes singular at the point *(x, y)* = (0, 0), and the transformation formulas becomes undefined there. With finite volume methods, it is possible to overcome this problem by using a special formula for the triangular shaped cells closest to the point (0, 0).

The blocking of the full domain is similar to unstructured domain decomposition, but with a difference that each block is further discretized in a structured manner. The first step in the multi-block structured grid generation is the definition of blocks of appropriate size and at correct location, and the step involves generating a structured grid for each block. An alternative to this procedure is the use of purely rectangular grids with objects "cut out" as holes in the grid, as shown in Fig. 4.7. With this approach however, it is hard to obtain a desired level of accuracy in the implementation of the boundary conditions. Furthermore, since cells are cut arbitrarily, there are chances that the boundary cells become distorted and very small, causing stability problems for explicit schemes.

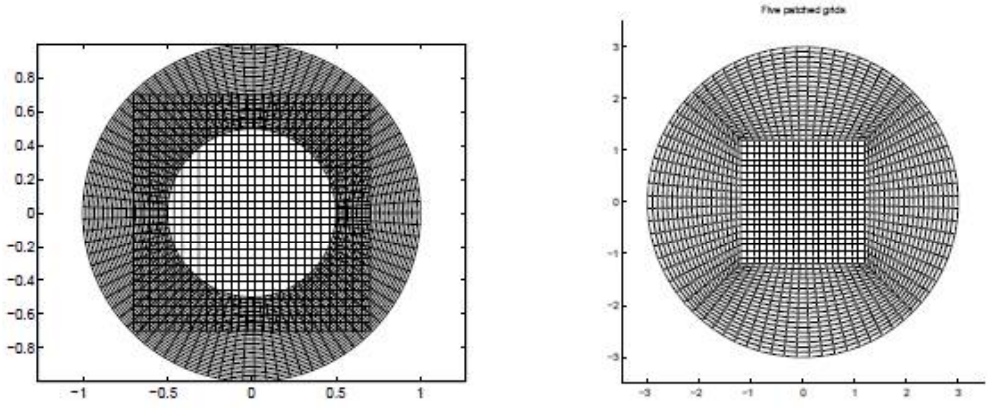

(a) Overlapping blocks (b) Adjacent blocks

Fig. 4.6: Different types of block arrangement

For the step of generating a single grid, there are some fairly general techniques. On the other hand, the division into blocks is usually done manually for each particular configuration, and can require many days work by an engineer.

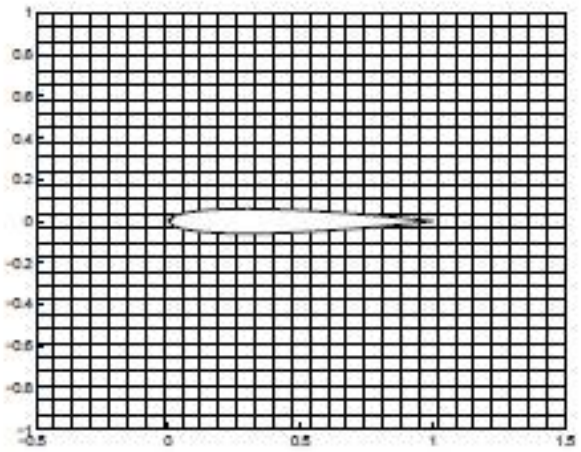

Fig. 4.7: Geometry cut out from a rectangular grid

In the current analysis the structured grids are prepared with the help of multi-blocking in ANSYS ICEMCFD software. ICEMCFD uses the concept of a separate blocking framework that is divided to represent the topology of the model and then associated to the specific model geometry. Structured hexagonal mesh is generated within each of the blocks and fit into the geometry. Then the meshes are converted into the unstructured form for solving the governing equation in ANSYS FLUENT 14.5. A couple of typical meshes for the geometries used in the current analysis are shown in Fig. 4.8 and Fig. 4.9.

The extents of the physical flow domain discretized and used for the analysis are given in Table 4.2. In Table 4.2, 'c' represents the chord length of the airfoil.

Table 4.2: Physical domain for flow solver

Front	1.0 c
Top	2.5 c
Bottom	2.5 c
Rear	4.0 c

For meshing for all the geometries, the multi-block structured grids are prepared with the help of ICEMCFD. The total number of elements for the both diamond and Busemann biplane airfoils are around 3.5×10^5 with a logarithmic stretching applied perpendicular to airfoil surface. The number of element is chosen such that the solution is independent of the number of elements. The boundary layer mesh has the first cell height of 8.11×10^{-6} m in order to resolve viscous stresses correctly.

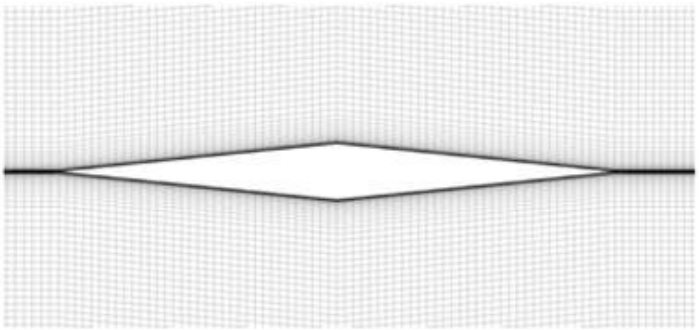

(a) Diamond Airfoil

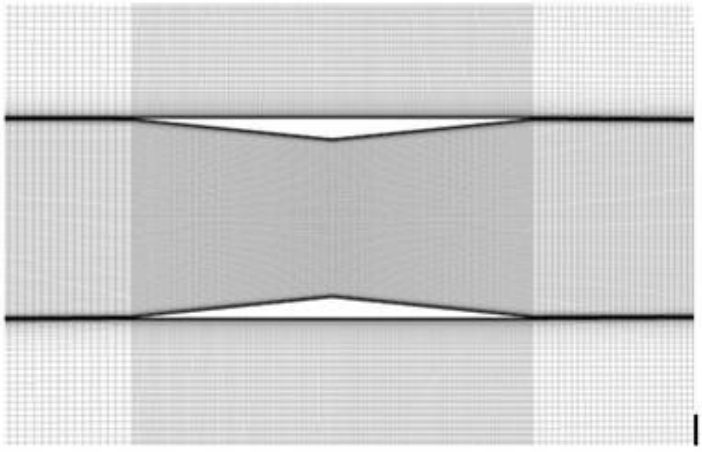

(b) Busemann Airfoil

Fig. 4.8: Multi-block grid around (a) diamond airfoil and (b) Busemann biplane airfoil

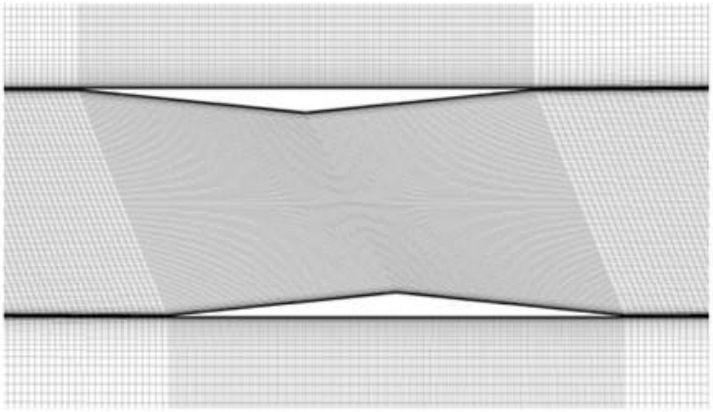

(a) Stagger Upper Element

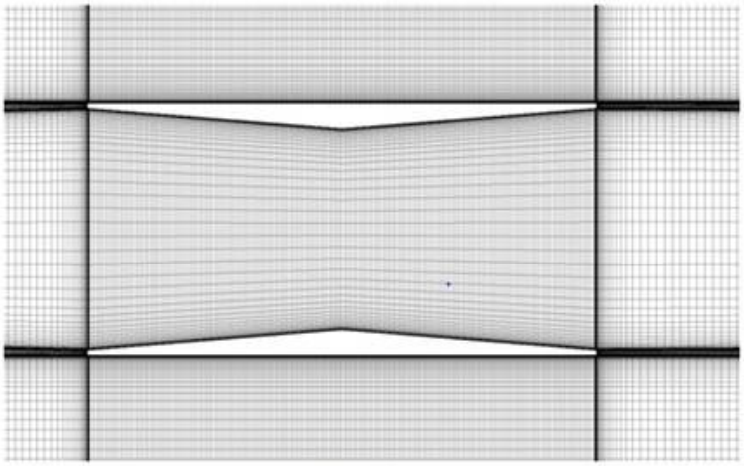

(b) Busemann Biplane with Leading Edge and Training Radius.

Fig. 4.9: Multi-bloc structured mesh around (a) staggered Busemann biplane and (b) Busemann biplane with rounded leading and trailing edges

4.9 Discretization

4.9.1 Temporal Discretization

ANSYS FLUENT uses a control-volume-based technique to convert a general scalar transport equation to an algebraic equation that can be solved numerically. The integral form of general finite volume method Eq. 4.1 can be written in the dual time stepping form for implicit time marching as in Eq. 4.16.

In Fluent, the discrete values of the fluid properties are stored at all cell centers. However, the face values are required for the convection terms in Eq. 4.16 and these values are obtained through the interpolation of the cell centre values. This is commonly accomplished using an upwind scheme. Fluent has several different schemes available, such as first-order upwind, second-order upwind, power law, and QUICK. The diffusion terms in Eq. 4.25 are central-differenced with second-order accuracy.

$$\frac{\partial}{\partial t}\int_{\Omega} \overrightarrow{W}\, d\Omega + \frac{\partial}{\partial \tau} W\, d\Omega + \oint_{\partial\Omega} \left(\vec{F}_c - \vec{F}_v\right) dS = \int_{\Omega} \vec{Q}\, d\Omega \qquad (4.25)$$

where t is physical time and τ is pseudo time. For dual time stepping, Eq. 4.25 is usually rearranged in the form given by Eq. 4.26.

$$\frac{\partial}{\partial \tau} W\, d\Omega = -\left[\frac{\partial}{\partial t}\int_{\Omega} \overrightarrow{W}\, d\Omega + \oint_{\partial\Omega} \left(\vec{F}_c - \vec{F}_v\right) dS\right] + \int_{\Omega} \vec{Q}\, d\Omega \qquad (4.26)$$

Theoretically the pseudo term on the left hand side of Eq. 4.26 should approach to zero at each time step before the physical time marches. On the right hand side, a steady state condition is satisfied before marching the physical time step. Temporal discretization is realized using the implicit second-order backward Euler scheme with an iterative procedure. The nonlinear coefficients are updated with each inner loop while the outer loop advances the solution in time. The separate spatial and temporal discretization of the governing equation, Eq. 4.12, leads for each control volume, to Eq. 4.27.

$$\frac{d\left(\Omega \overline{M} \overrightarrow{W}\right)}{dt} = -\vec{R}_I \qquad (4.27)$$

where Ω incorporates the volume, $\vec{R}_I$ denotes the residual (i.e. the complete spatial discretization including the source term), $\overline{M}$ is the mass Matrix, and index I means the particular control volume. Eq. 4.27 has to be iterated in time to obtain a steady-state solution ($\vec{R}_I = 0$), or to reproduce the time history of an unsteady flow. For unsteady flows, the 3-point backwards Euler scheme with second-order

accurate temporal discretization, as given in Eq. 4.28 is used.

$$\frac{3(\Omega\bar{M})_I^{n+1}\vec{W}_I^{n+1} - 4(\Omega\bar{M})_I^{n}\vec{W}_I^{n} + (\Omega\bar{M})_I^{n-1}\vec{W}_I^{n-1}}{2\Delta t} = -\vec{R}_I^{n+1} \qquad (4.28)$$

In Eq. 4.28, Δt denotes the global physical time step. The superscript $n+1$ represents the value at next time level, i.e. $t+\Delta t$, n is the value at the current time level, i.e. t, and $n-1$ is the value at the previous time level, i.e. $t-\Delta t$.

4.9.2 Spatial Discretization

Based on the grid, control volumes are defined in order to evaluate the integrals of the convection and viscous fluxes as well as the source term. The time derivative of the conservation variables $\vec{W}$ can be written as:

$$\frac{\partial \vec{W}}{\partial t} = -\frac{1}{\Omega}\left[\oint_{\partial\Omega}(\vec{F}_c - \vec{F}_v)dS - \int_{\Omega}\vec{Q}\, d\Omega\right] \qquad (4.29)$$

The surface integral on the right hand side of Eq. 4.29 is approximated by a sum of the fluxes crossing the faces of the control volume. This approximation is called spatial discretization. It is usually supposed that the flux is constant along the individual face and is evaluated at the middle of the surface. The source term inside the control volume is assumed to be constant. Therefore, for a particular control volume, $\Omega_{I,J,K}$, Eq. 4.29 can be written as:

$$\frac{d\vec{W}_{I,J,K}}{dt} = -\frac{1}{\Omega_{I,J,K}}\left[\sum_{m=1}^{N_f}\left(\vec{F}_c - \vec{F}_v\right)\Delta S_m - \left(\vec{Q}\,\Omega\right)_{I,J,K}\right] \qquad (4.30)$$

The I,J,K in the Eq. 4.30 represents the control volume in computational space, N_f are the number of faces around a control volume ($N_f = 6$ for 3d case). The variable ΔS_m stands for the area of the face m. The term inside the square bracket on the right hand side of Eq. 4.30 is usually called the residual which can be written as:

$$\frac{d\vec{W}_{I,J,K}}{dt} = -\frac{1}{\Omega_{I,J,K}}\vec{R}_{I,J,K} \tag{4.31}$$

$$\text{where, } \Omega_{I,J,K} = \frac{1}{3}\sum_{m=1}^{m=6}\left(\vec{r}_{mid}\cdot\vec{S}\right)_m$$

$$with, \quad \vec{S}_m = \begin{bmatrix} S_{x,m} \\ S_{y,m} \\ S_{z,m} \end{bmatrix} = \vec{n}_m\,\Delta S_m$$

$$and \quad \Delta S_m = \left|\vec{S}_m\right| = \sqrt{S_{x,m}^2 + S_{y,m}^2 + S_{z,m}^2}$$

For a 3D cell with a control volume, $\Omega_{I,J,K}$, $\vec{r}_{mid}$ denotes the midpoint of the control volume face m (i.e. for a 3D cell, number of faces $m = 6$), ΔS_m in Eq. 4.31 is the area of the face m, and $\vec{r}$ is the location in space of some point of the control volume Ω which can be written as $\vec{r} = \left[r_x, r_y, r_z\right]^T$.

The cell-centre scheme, as shown in Fig. 4.1(b) has been used in Fluent, wherein the control volumes are identical to the grid cells and the flow variables are associated with their centroids. Thus, the cell face $\vec{n}_{I+1/2,J,K}$ is the face between cell I,J,K and $I+1,J,K$ in Fig.4.1(b). Therefore, the convective fluxes through the face $(I+1/2\,,J,K)$ is as given by Eq. 4.32.

$$\left(\vec{F}_c\Delta S\right)_{I+1/2,J,K} \approx \vec{F}_c\left(\vec{W}_{I+1/2,J,K}\right)\Delta S_{I+1/2,J,K} - \vec{D}_{I+1/2,J,K}$$

$$\vec{W}_{I+1/2,J,K} = \frac{1}{2}\left(\vec{W}_{I,J,K} + \vec{W}_{I+1,J,K}\right) \tag{4.32}$$

where $\vec{D}$ is the artificial dissipation which is added to the central fluxes for stability.

The discretization of the viscous flux $\vec{F}_v$ in Eq. 4.32 is often calculated from cell interface value. The AUSM (Advection Upstream Splitting Method) scheme is used for calculating the variables on the cell. Here too, the flux is split into two separate components so that each one may be properly upwind stenciled. Liou and Steffen [60] are the original authors of this technique, which has been improved and altered several time both by them and by others as well [60]. In the

original AUSM scheme, the flux term is split into two parts, the convective flux and the pressure flux as given in Eq. 4.33.

$$\vec{F} = F_C + F_P = \begin{pmatrix} \rho u \\ \rho u^2 \\ \rho u h_0 \end{pmatrix} + \begin{pmatrix} 0 \\ P \\ 0 \end{pmatrix} \tag{4.33}$$

The convective flux is carried by the flow, i.e. through the entropy wave. It can be defined completely in the upwind direction by using the properties of the convective (entropy) wave. The pressure term of the flux is the term that is carried by the entropy waves, which allow for travel in a direction against the flow in a subsonic situation. The convective term is thus separated into two relative contributions. First of the two, the convective fluxes are evaluated at the interface as given by Eq. 4.34.

$$\vec{F}_C = M_{1/2} \begin{Bmatrix} \rho a \\ \rho u a \\ \rho a h_0 \end{Bmatrix}_{(L \, or \, R)} \tag{4.34}$$

The special Mach number term that has been pulled out of the convective flux term is the "convective" Mach number. The convective Mach number is a measure of the effective convective potential of the flow, based on the strength of the entropy eigenvalue. The convective Mach number can be defined as in Eq. 4.34.

$$M_{1/2} = M_L^+ + M_R^- \tag{4.35}$$

The definitions for the left and right Mach numbers are taken from the Van Leer method [60], as in Eq. 4.36.

$$M^{\pm} = \begin{cases} \pm\frac{1}{4}(M \pm 1)^2 & if \; |M| \leq 1 \\ \frac{1}{2}(M \pm |M|) & if \; |M| > 1 \end{cases} \tag{4.36}$$

This equation shows that the convective Mach simply reduces to the full signed Mach number for any supersonic flow, while it employs Van Leer's Mach number

splitting for subsonic flows. The convective Mach number definition is one of the key variations between the successive AUSM enhancements. The "L or R" in the remaining flux term is a switch that corresponds to the sign of the convective Mach number as defined in Eq. 4.37.

$$\begin{Bmatrix} \rho a \\ \rho u a \\ \rho a h_0 \end{Bmatrix}_{(L\,or\,R)} = \begin{cases} \{\ \}_{LEFT} & if\ M_{1/2} \geq 0 \\ \{\ \}_{RIGHT} & if\ M_{1/2} < 0 \end{cases} \tag{4.37}$$

In this way, the upwind convective flux is defined based on the convection Mach number of the flow. The pressure term is treated separately. It is defined such that the communication in both directions may be admitted. Eq. 4.38 shows the calculation of the pressure flux.

$$P = P_L^+ + P_R^- \tag{4.38}$$

The left and right pressure terms are defined by using second order polynomial functions of the acoustic speeds. Liou and Steffen (1993) also give a slightly simpler first order polynomial splitting, but the second order scheme, given in Eq. 4.39, is used here.

$$P^{\pm} = \begin{cases} \pm\frac{P}{4}(M \pm 1)^2(2 \mp M) & if\ |M| \leq 1 \\ \frac{P}{2}\frac{(M \pm |M|)}{M} & if\ |M| > 1 \end{cases} \tag{4.39}$$

Again the pressure term becomes the full signed upwind pressure for any supersonic flow. For subsonic flow, the pressure correctly shows characteristics for both upwind and the downwind waves. The fluxes at any cell boundary then become defined by Eq. 4.40, with supplementary definitions given in Eq. 4.36 and Eq. 4.32.

$$\vec{F} = (M_L^+ + M_R^-)\begin{Bmatrix} \rho a \\ \rho u a \\ \rho a h_0 \end{Bmatrix}_{(L\,or\,R)} + \begin{Bmatrix} 0 \\ P_L^+ + P_R^- \\ 0 \end{Bmatrix} \tag{4.40}$$

This defines the flux terms necessary to evaluate the explicit residual. For implicit schemes, the Jacobian of the flux must be computed since the left and right pressure and convective Mach number values shown in Eq. 4.40 are only functions of the corresponding one-sided state. Eq. 4.41 and 4.42 give the left and right derivatives for any term in the Jacobian matrix.

$$\frac{\partial \vec{F}}{\partial q_j^{LEFT}} = (M_L^+ + M_R^-)\frac{\partial}{\partial q_j^L}\begin{Bmatrix}\rho a\\ \rho u a\\ \rho a h_0\end{Bmatrix}_L + \frac{\partial M_L^+}{\partial q_j^L}\begin{Bmatrix}\rho a\\ \rho u a\\ \rho a h_0\end{Bmatrix}_{(L\,or\,R)} \tag{4.41}$$

$$\frac{\partial \vec{F}}{\partial q_j^{RIGHT}} = (M_L^+ + M_R^-)\frac{\partial}{\partial q_j^R}\begin{Bmatrix}\rho a\\ \rho u a\\ \rho a h_0\end{Bmatrix}_R + \frac{\partial M_R^+}{\partial q_j^R}\begin{Bmatrix}\rho a\\ \rho u a\\ \rho a h_0\end{Bmatrix}_{(L\,or\,R)} \tag{4.42}$$

The first term in each derivative becomes zero if the switch does not indicate the respective direction, i.e. if the convective Mach number is positive, the convective flux will be *"LEFT"* biased and the derivative of the flux with respect to the right state goes to zero by definition. Thus in this case, the first term of Eq. 4.42 becomes zero. However, the second term remains non-zero since is an actual term instead of a derivative. For supersonic flows, the second and third terms goes to zero for the downwind side of the flow. The actual derivatives with respect to the face conservative variables for the pressure, Mach number, and flux terms are relatively straight forward by employing the chain rule.

4.10 Initial and boundary condition

The physical boundary condition is the utmost important aspect of the problem and needs to be applied correctly for simulating real life situations. This is because of the nature of the equations and their domains of dependence and zones of influence have implications for boundary conditions. The governing equations described above are very generic and do not change from one problem to another. Therefore, apart from these conservation equations, initial and boundary conditions are needed to define a problem. Initial conditions are specified by assigning the density, flow velocities and pressure everywhere in the solution

region before the start of the solution procedure. Typically the initial conditions are set such that the density, pressure and flow velocities are freestream values.

The two common boundary conditions for an external flow are the wall boundary condition and the farfield boundary condition. Wall boundaries are the natural boundaries of the physical domain which arise from the wall surfaces being exposed to the flow. At the surface of the boundary, the relative velocity between the fluid and the solid wall is zero, in the case of the viscous fluid. The truncation of the physical domain or system for the purpose of numerical simulation leads to artificial far-field boundaries, where certain physical quantities have to be prescribed. The farfield boundary condition has to fulfill two basic requirements, first, the effect of the outer flow region must not reflect back to the main flowfield region selected for the numerical calculations, and secondly the domain truncation should have no notable effect as compared to the infinite domain on the flow solutions.

4.8.1 Wall Boundary Condition

In this work, all the solid walls are treated as viscous wall. Therefore no-slip condition is applied, which requires the fluid velocity at the wall be equal to the surface velocity. In a viscous flow, the flow velocity between the wall surface and the fluid is assumed to be zero. It is called no-slip condition. For a stationary surface in a two-dimensional Cartesian system, this condition can be described as:

$$u_w = v_w = 0 \text{ at } y = 0$$

4.8.2 Far-field Boundary Condition

Fig. 4.10 shows a typical example of the CFD domain with different boundaries condition applied. The pressure farfield boundary condition is applied on the inlet, outlet, top and bottom surfaces and the magnitude of the flow parameters are stipulated at the inlet and on top and bottom farfield boundaries. The value of various parameters stipulated or calculated on the farfield conditions are given in table 4.3.

The farfield boundary on the background mesh is placed as far away in the radial direction from body surfaces as computationally feasible such that the conditions at these mesh points are very close to freestream.

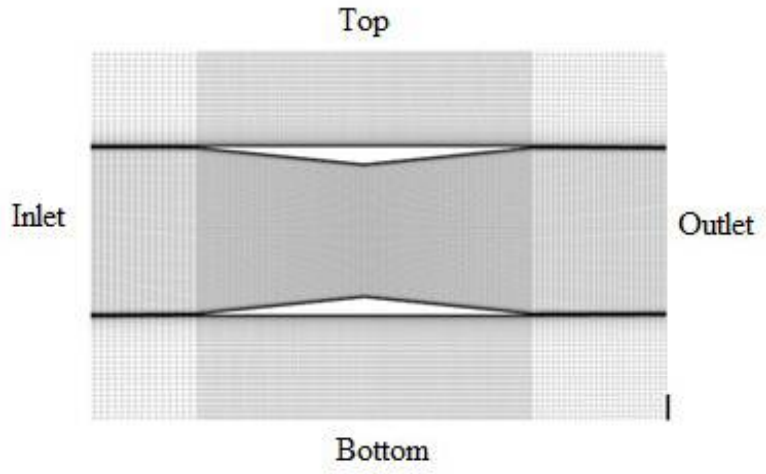

Fig. 4.10: Farfield boundary conditions for domain around Busemann biplane.

Table 4.3 Farfield boundary condition

	Symbol	Units	Values
Mach Number	M	-	0.5 – 2.5
Temperature	T	K	288.16
Pressure	P	N/m2	101325.0
Turbulent viscosity ratio	μ_T/μ	-	2.0
Molecular viscosity	M_e	Kg/ms	1.7895×10^{-5}
Reynolds number	Re	-	$1.14 \times 10^7 - 5.78 \times 10^7$

4.9 Grid independent Study

The number of element is chosen such that the solution is independent on the no of elements. Figure 4.11 shows the variation of Drag coefficient with number of

grid, and is found that the solution becomes independent of the number of elements for grids with more than 3.5 x 10^5 elements. The boundary layer mesh has the first cell height of 8.11 x 10^{-6}m in order to resolve viscous stresses correctly. The results is calculated at standard sea level condition of pressure 101325 N/m^2, temperature 300 K, density 1.1766 kg/m^3 and viscosity 1.7894e^{-5} kg/m-s.

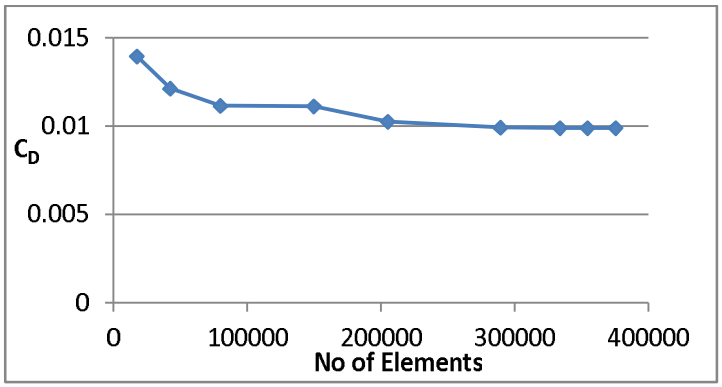

Fig. 4.11: Variation of drag coefficient with number of elements for the Busemann airfoil.

4.10 Solver Validation

As a part of the solver validation studies, the validations of the mathematical models used and the numerical schemes selected in the state of the art CFD software ANSYS FLUENT 14.5, the standard diamond airfoil and the Busemann type biplane configuration are studied under non lifting conditions at supersonic speeds. The results obtained for these two cases are compared with the theoretical values that are calculated using the shock expansion theory. The flow structures for the two cases are also compared with the flow patterns reported in the literature.

4.10.1 Diamond and Original Busemann biplane

In this section the aerodynamics characteristics viz. the lift and drag coefficients, of the diamond and Busemann type biplane configuration at non lifting conditions are studied. The geometrical dimensions for the both airfoils are taken in such a

way that, the overall volume of the body remains same for the easy comparison of the results between the two cases. For the diamond airfoil the thickness/chord ration is taken as 0.05, whereas for the each element of the Busemann biplane the thickness/chord ratio is set to be 0.05. In order the get the minimum wave drag for the Busemann type biplane (at M_∞ = 1.7), the distance between the elements is chosen as 0.5c, and the angle of attack for both the airfoils is set to zero. The multi-block structured grids are prepared with the help of ICEMCFD software and then converted into unstructured as discussed in the section 4.6.2. The total number of elements for the both diamond and Busemann airfoils are around 3.5 million and are stretched perpendicular to airfoil surface so as to resolve the viscous stresses. The results are obtained through numerical solution of 2 dimensional Navier-Stokes equations in ANSYS FLUENT 14.5 with the boundary conditions discussed in the previous section. A second order accurate, steady state results are obtained through time marching solution of coupled, 2-dimesional Navier-Stokes equations using FLUENT. Spalart-Allmaras (SA) turbulent model (one equation model) is used for both the configuration to predict the effect of turbulence and for the calculation of turbulent viscosity.

The results for lift and drag coefficients obtained from the numerical simulations are compared with the standard supersonic thin airfoil theory at M_∞ = 1.7 and are given in Table 4.4. From the comparison of these results, we can say that the results obtained from the numerical simulation are good agreement with the analytical results.

Table 4.4 Numerical and Theoretical lift and drag coefficients of diamond and Busemann airfoil.

	Theoretical results		Numerical results	
	C_L	C_D	C_L	C_D
Diamond	0.0000	0.0291	0.0000	0.0301
Busemann	0.0000	0.0000	0.0000	0.00989

The magnitude of the drag coefficient for the Busemann type biplane is lower than the standard Diamond airfoil at M_∞ = 1.7, this mainly because of the wave

cancellation and reflection between the elements. However the drag coefficient cannot be completely eliminated due to the presence of the boundary layer effect. Fig. 4.12 and 4.13 shows the variation of C_p (pressure coefficient) and the Mach numbers at $M_\infty = 1.7$, for the Diamond and Busemann type biplane configuration.

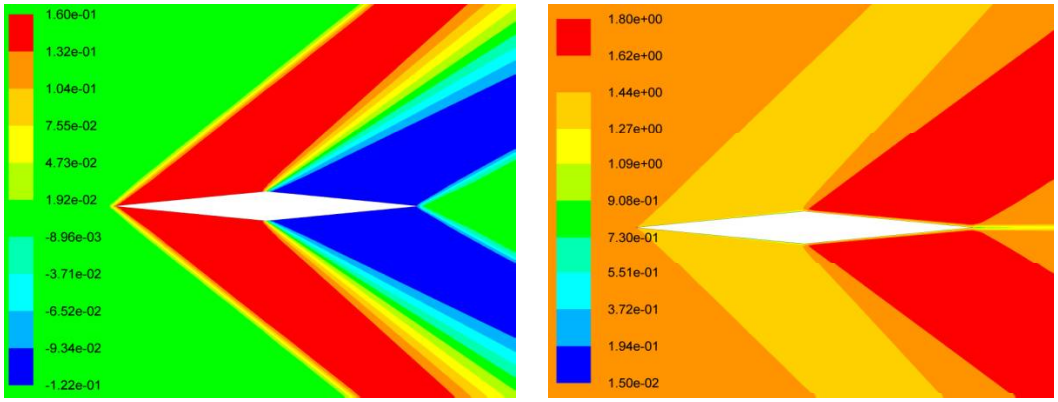

(a)C_p variation (b)Mach number Variation

Fig. 4.12: C_p and Mach number variation for Diamond airfoil at $M_\infty = 1.7$

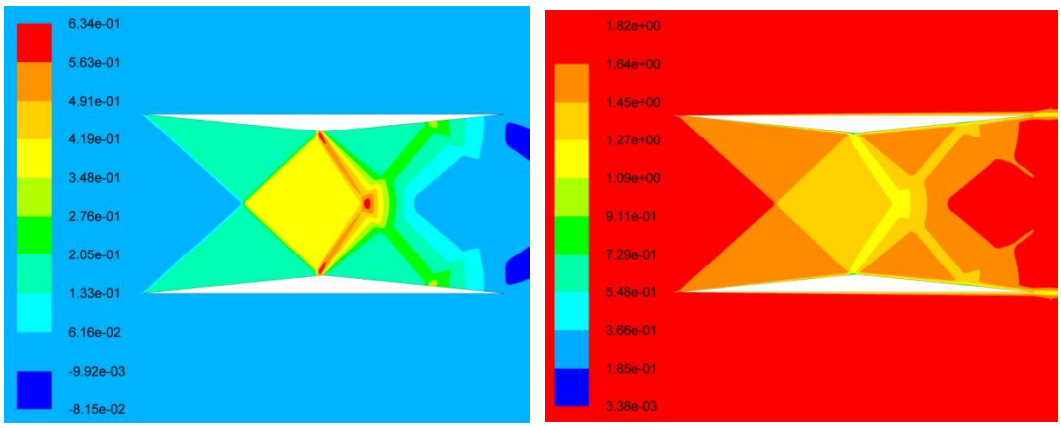

(a) C_p Variation (b)Mach number Variation

Fig. 4.13: C_p and Mach number variation for Busemann airfoil at $M_\infty = 1.7$

Next, the behavior of the Busemann biplane at Mach numbers other than the design Mach number 1.7 is examined. In subsonic case, the high pressure region is developed before the throat of the section due to the compression effect and after the throat of the section; the pressure decreases due to the expansion of the

flow generating a significant amount of pressure drag. The region of low pressure aft of the mid-section is expands with increasing freestream Mach number and further increment in the pressure drag is observed with increasing Mach numbers.

As can be seen in Fig. 4.14 the maximum pressure coefficient value of 0.357 at $M_\infty = 0.5$ increases to 1.29 at $M_\infty = 1.0$. The main cause of this pressure increment is the compression effect between the element and the larger region of high pressure ahead of the mid-section of the Busemann biplane elements, as a results the overall drag component is increases from 0.0167 at $M_\infty = 0.5$ to a value of 0.1283, at $M_\infty = 1.0$.

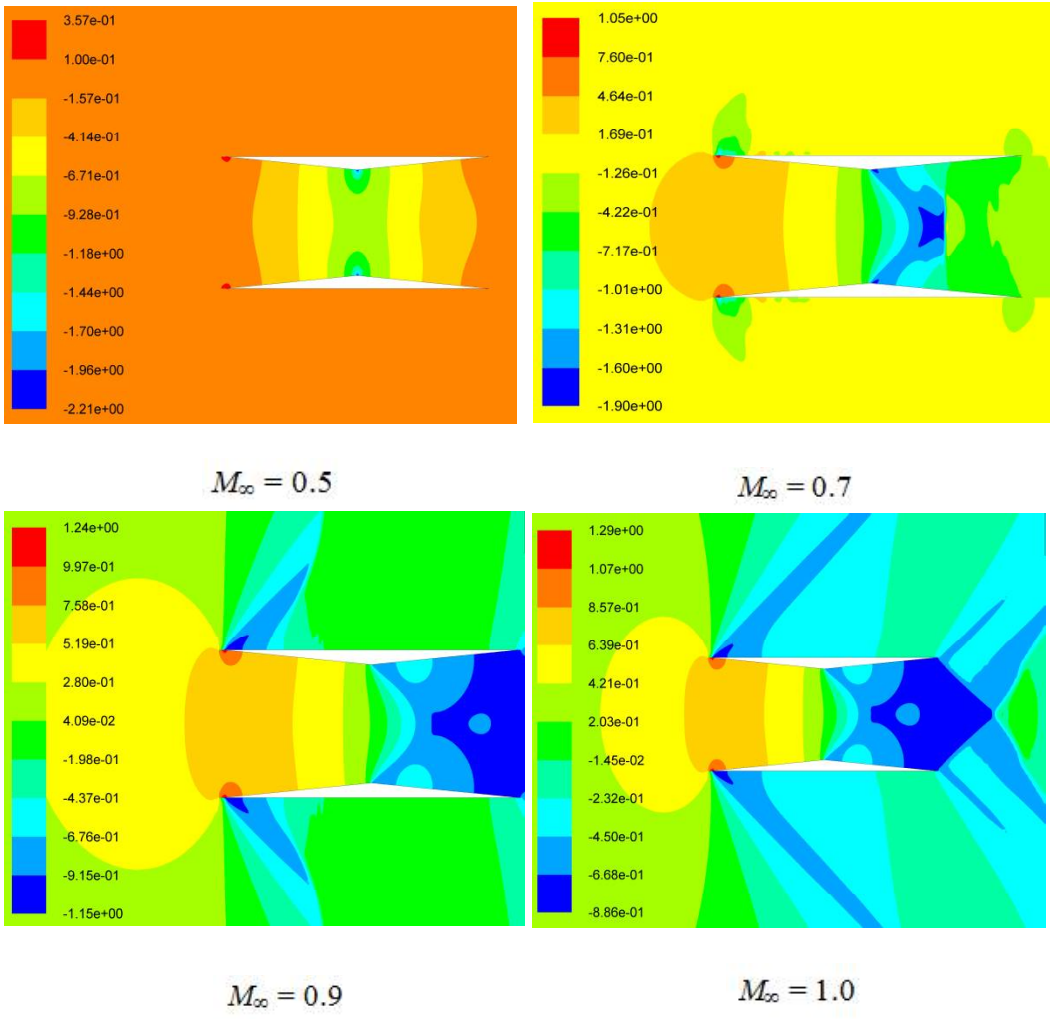

Fig. 4.14: Contours of C_p for Busemann biplane at $0.5 \leq M_\infty \leq 1.0$

In the case of supersonic flow at $M_\infty = 1.2$, due to the compression effect between the Busemann biplane elements, a strong bow shock wave is generated in front of the body. With the further increment in the freestream Mach number the bow shock wave moves closer to the body and the losses across the shock wave increases with subsequent rise in the static pressure aft of the shock wave as can be seen in Fig. 4.15. This creates a large region of high pressure region between the biplane elements ahead of the mid-section. As a result the drag coefficient of 1.38 at $M_\infty = 1.2$ increases to a value of 1.54 at $M_\infty = 1.6$.

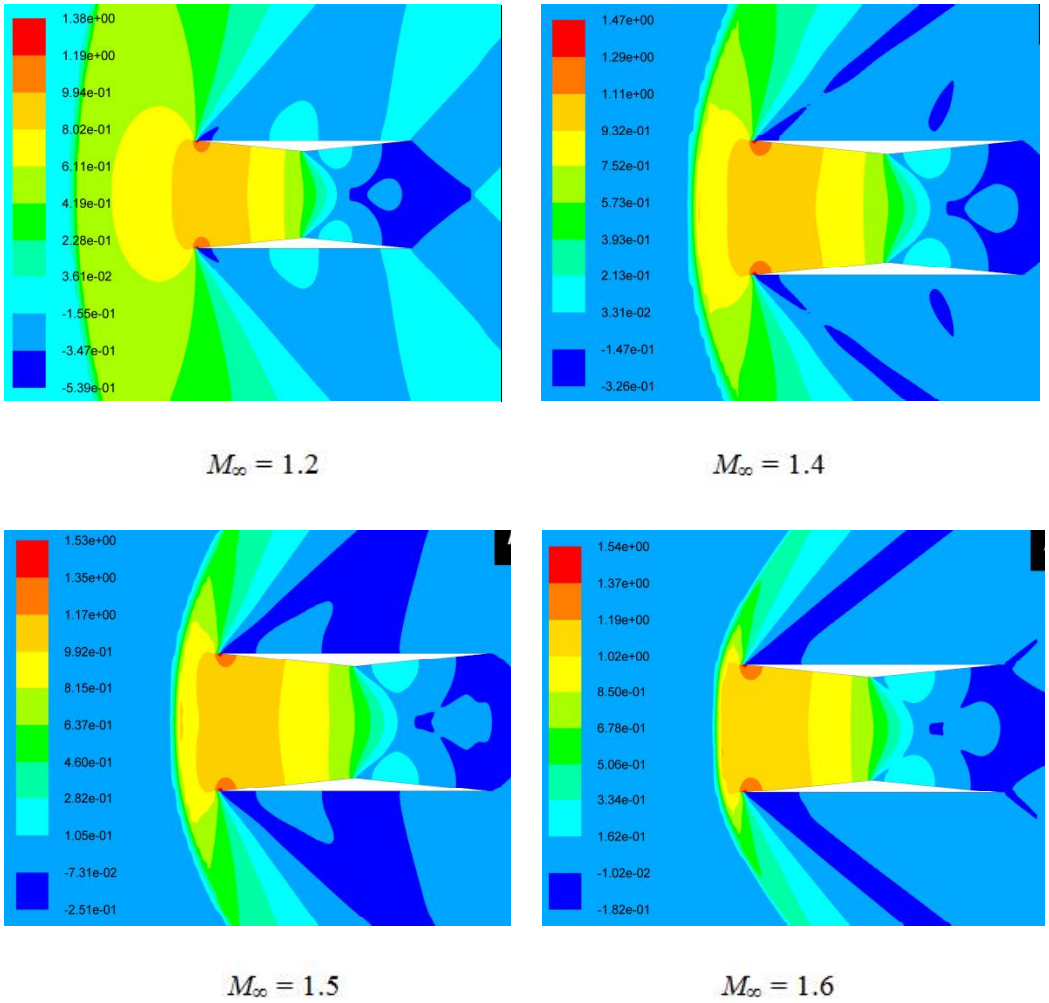

Fig. 4.15: Contours of C_p for Busemann biplane at $1.2 \leq M_\infty \leq 1.6$.

With a further increment in the Mach number, i.e. M_∞ = 1.7, the detached shock wave becomes attached to the body and the pressure aft of the shock wave reduces slightly due to formation of an oblique shock wave and a decrease in the pressure drag is observed. Due to the symmetrical positioning of the upper and lower element of the Busemann biplane the strength of the attached right running shock wave is eliminated by the left running shock wave due cancellation and reflection between the elements and the pressure drag is reduced to a value of 0.00989 at the free stream Mach number 1.7. The pressure variation between the biplane elements at a freestream Mach number of 1.7 is shown in Fig. 4.13.

With further increment in the free stream Mach number ($M_\infty > 1.7$), the shock wave angle at the leading edge of the elements is decreased and the shock-shock interaction point moving backwards. The expansion waves generated at the throat of the biplane interacts with the shock waves decreasing the pressure behind the throat of the section, hence increasing the pressure drag for the section. With further increment in the Mach number, the shock interaction point between the element further moves downwards and further reduction in the pressure aft of the mid-section and an increase pressure drag for the combination. The contours of pressure coefficients for various Mach numbers above 1.7 are shown in Fig. 4.16.

The shock-shock interactions between the biplane elements govern the drag of Busemann biplane. The detailed variation of drag coefficient for diamond airfoil and the Busemann biplane configuration for a wide range of freestream Mach numbers ($0.5 \leq M_\infty \leq 2.5$) are given in Fig. 4.17.

From the plot we can conclude that the Busemann type biplane configuration provides the lowest drag at M_∞ =1.7, and the drag coefficient are lower than the Diamond airfoil for the range of Mach numbers from 1.7 to 2.5. The Busemann type biplane configuration shows the better performance (low drag coefficient) at supersonic speeds ($1.7 \leq M_\infty \leq 2.5$), but the performance is poor at lower Mach

Numbers ($M_\infty \leq 1.6$) due to the flow chocking phenomenon and the magnitude of the drag coefficient is greater than the Diamond airfoil.

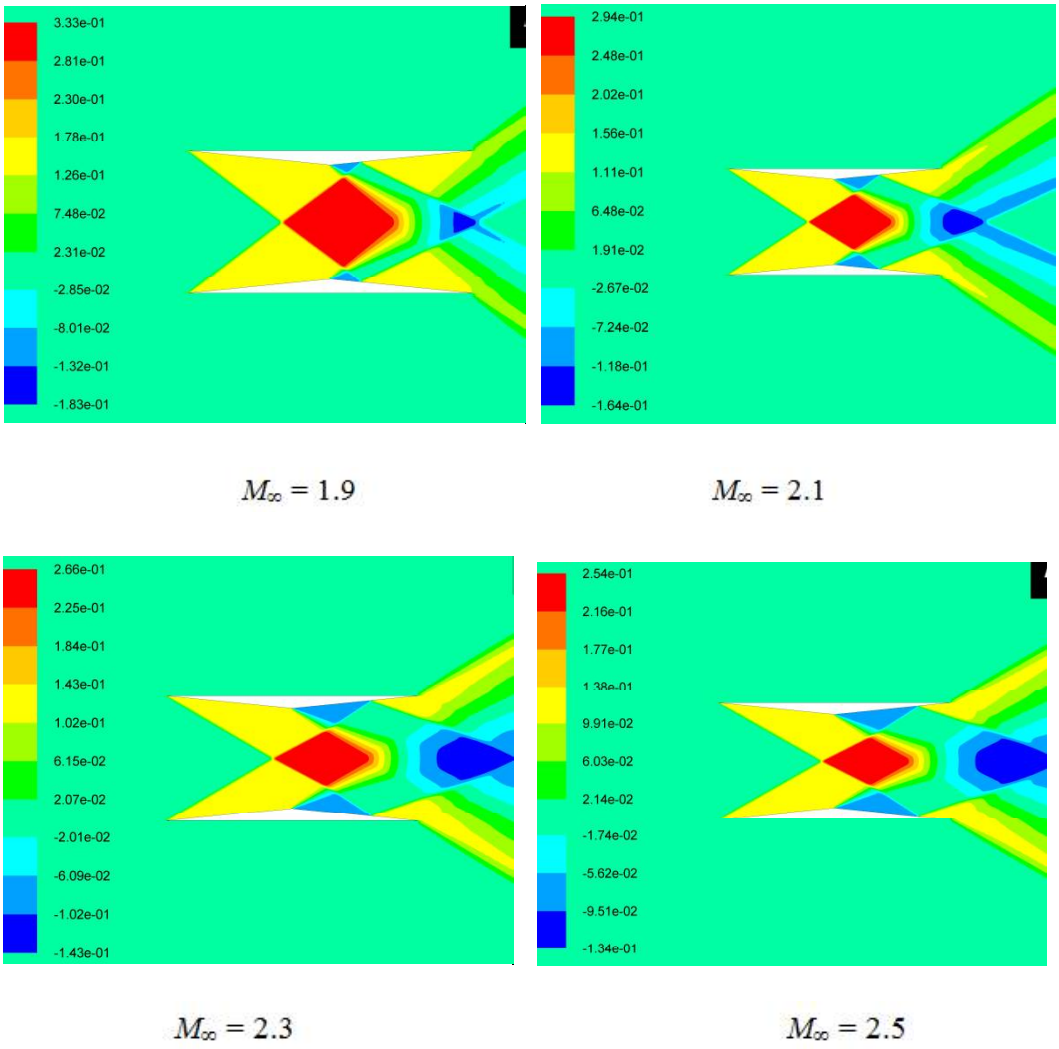

Fig. 4.16 C_p variation of Busemann biplane for $1.9 \leq M_\infty \leq 2.5$.

The drag coefficients for both diamond airfoils and Busemann biplane at various freestream Mach numbers obtained numerically are in close agreement with those reported in the literature and with those calculated using the shock-expansion theory. The numerically values of drag coefficients at zero lift differ from the analytical values by less than a percent. The difference in lift and drag coefficients observed is because of the viscous model of the flow as the shock-expansion

theory is based on inviscid model of flow. The shock-shock interaction shown in Fig. 4.16 matches closely with those reported in literature [9, 10]. The numerical methodology opted for the study of the aerodynamic characteristics of modified Busemann biplane thus, can provide reliable results within the limitations of computational assumptions.

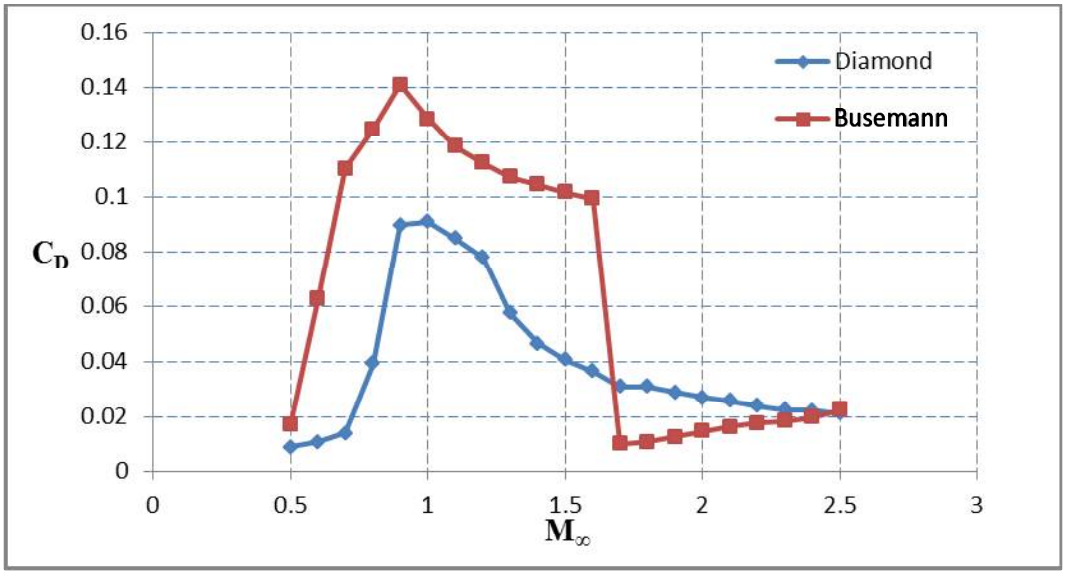

Fig. 4.17 C_D variation with freestream Mach number for Diamond and Busemann airfoil at zero-lift condition.